Transient X-ray Diffraction Reveals Non-Equilibrium Phase Transition in

Thin Films of CH₃NH₃PbI₃ Perovskite

Shobhana Panuganti^a, Shelby A. Cuthriell^a, Ariel A. Leonard^a, Michael A. Quintero^a, Craig C. Laing^a, Burak Guzelturk^b, Xiaoyi Zhang^b, Lin X. Chen^{a,c}, Mercouri G. Kanatzidis^{a,c}, Richard D. Schaller^{a,d*}

^aDepartment of Chemistry, Northwestern University, Evanston, IL 60208, USA

Abstract

Advantageous optoelectronic properties of methylammonium lead triiodide likely arise from coupling between photogenerated charge-carriers and the soft, deformable lattice. We investigate structural dynamics of MAPbI₃ films using time-resolved X-ray diffraction versus pump-probe time delay and pump intensity. During the first nanosecond, the lattice anisotropically distorts from tetragonal to cubic at excitation intensities that are insufficient to thermally induce the first-order thermodynamic phase transition at 330K. The high-symmetry structure then relaxes back to the starting phase with 11 and 236-ns time constants via a different transition pathway than observed either in the first nanosecond or in previous reports for MAPbI₃. Early-time dynamics are consistent with polaron formation and lattice strain stabilization while the slower recovery dynamics outlive radiative recombination and relates metastability. Fluence-independence of these lattice deformations in the low-power regime conveys relevance to optoelectronics including photovoltaics and highlights sustained involvement of non-equilibrium, photoinduced lattice reorganization in MAPbI₃ under functional conditions.

^bX-ray Sciences Division, ^cMaterials Science Division, and ^dCenter for Nanoscale Materials, Argonne National Laboratory, Lemont, IL 60439, USA

^{*} Corresponding author: schaller@anl.gov, schaller@northwestern.edu

Significant research efforts focus on methylammonium lead iodide and related hybrid organic-inorganic perovskites because they are inexpensive, solution-processable semiconductors with desirable properties for optoelectronic applications. 1-3 Recent studies have suggested that many of these unexpected and attractive properties likely arise from dynamic structural behavior not observed in more rigid crystalline substances^{4,5} allowing for complex lattice-carrier coupling, such as the rapid formation of polarons.⁶⁻⁹ While there are reports that the operative conditions of optoelectronic applications do affect the structure and optical properties of this material, transient spectroscopic studies are unable to directly probe underlying lattice behavior, which is typically assumed not to change appreciably.^{5,10,11} When lattice behavior deviates significantly from equilibrium, such as we show here with MAPbI₃, electronic phenomena respond to the altered crystal symmetry, thus spectroscopic findings can misinterpret observables that actually derive from lattice evolution. In the same way that crystal phase transitions can alter bandgap and carrier effective mass, local changes in crystal symmetry near photon absorption events can yield carrier trapping, but also screening and protection of charges from rapid recombination.^{8,12} Direct investigations of lattice dynamics with high Q resolution are required to discern conditions that lead to lattice changes and relevant timescales of distortion formation and relaxation. Photoinduced heating can also occur due to intraband relaxation of hot carriers and Auger processes, such as from above-gap excitation, 13-15 introducing both thermal and electronic effects to consider in the overall lattice response. 11,16,17

Prior structural studies of MAPbI₃ have determined that this material undergoes a first-order thermodynamic phase transition from the room-temperature tetragonal I4/mcm space group into the high-temperature cubic $Pm\overline{3}m$ phase. Single crystal diffraction has shown that the two structures are closely related with additional distortions present in the tetragonal structure that

lower its symmetry.^{10,19} In particular, the Pb-I-Pb bond angles are 180.0(0)° and 179.1(4)° whereas the tetragonal lattice distorts away from this "ideal" bonding geometry (see Figure 1a).²⁰ One recent study utilizing ultrafast electron diffraction observed large increases in disordered motion of organic cation and halide site occupancy, providing further evidence of non-equilibrium structural changes.²¹ Still, currently available transient electron diffraction techniques lack sufficient resolution to discern individual Bragg reflections, which could offer insight into the response along specific crystallographic directions in the lattice and clarify key aspects of its structural lability.²²

In this work, we perform time-resolved X-ray diffraction measurements of MAPbI₃ thin films that reveal significant, non-equilibrium distortions following photoexcitation with fluence independence that suggests relevance to solar energy conversion. Unlike other techniques, powder X-ray diffraction of thin films using pulsed (79 ps), synchrotron X-rays affords high-resolution diffraction for time-resolved structural insights and individually resolved Bragg reflections that can be monitored with respect to pump-probe delay time. By using pulsed excitation, we are able to examine the fundamental carrier and lattice dynamics that underlie material performance with aims to comprehend and eventually guide optoelectronic materials design. We observe fluenceindependent, structural transformations of MAPbI₃ that indicate gradual, anisotropic distortions of the lattice from tetragonal to a distinct cubic phase followed by a slow recovery back into the tetragonal phase. Notably, while our observations are consistent with reported photoinduced phase transitions in metal halide perovskites,²³ our results also suggest that the material recovery from the high-symmetry structure back to the unexcited, tetragonal phase proceeds through structural distortions unlike those observed during the rise process in the first nanosecond. These findings establish a more precise understanding of the dynamic excited-state response in MAPbI₃, offer

insight into the atypical, non-equilibrium behaviors that enable its remarkable performance, and provide clear evidence that the remarkable *in-situ* material properties arise from the unique structure of the operative material, which is not the same as the equilibrium structure.

Measurements were conducted at Beamline 11-ID-D of the Advanced Photon Source at Argonne National Laboratory according to the setup shown in Figure S1. Thin films of MAPbI₃ were fabricated using modified, published methods.²⁴ Briefly, MAPbI₃ crystals were synthesized and dissolved in dimethylformamide to produce a precursor solution for spin-coating onto sapphire substrates. Substrates were then annealed to produce polycrystalline thin films and coated with polymethyl methacrylate. Films were photoexcited using 400 nm (3.1 eV), 1.2 ps duration pulses at 10 kHz with controlled fluences for a pump spot area of 1200 x 6900 microns of above-gap excitation. Notably, the above-gap excitation homogeneously excites within the plane of the film and is not selective for particular film regions. Films were rapidly spun in order to reduce degradation, present spatially averaged responses, and excite regions of the sample that are under ambient conditions X-ray diffraction probing was performed using 11.7 keV X-ray pulses that were 79 ps in duration, and powder diffraction patterns for given pump-probe time delays were integrated on a Pilatus 2M detector. To lessen photodegradation over the course of the experiments, we prepared sample films with thicknesses >0.5 µm, therefore larger than the penetration depth of the pump but within X-ray probing depth. By subtracting the steady-state diffraction pattern of the sample from each transient photoexcited pattern, we isolated the behavior of the photoexcited population from the unexcited depth of the film. Throughout this work, we refer to these post-processed, differenced patterns as transient patterns for ease of analysis. Additional details are available in the Supporting Information.

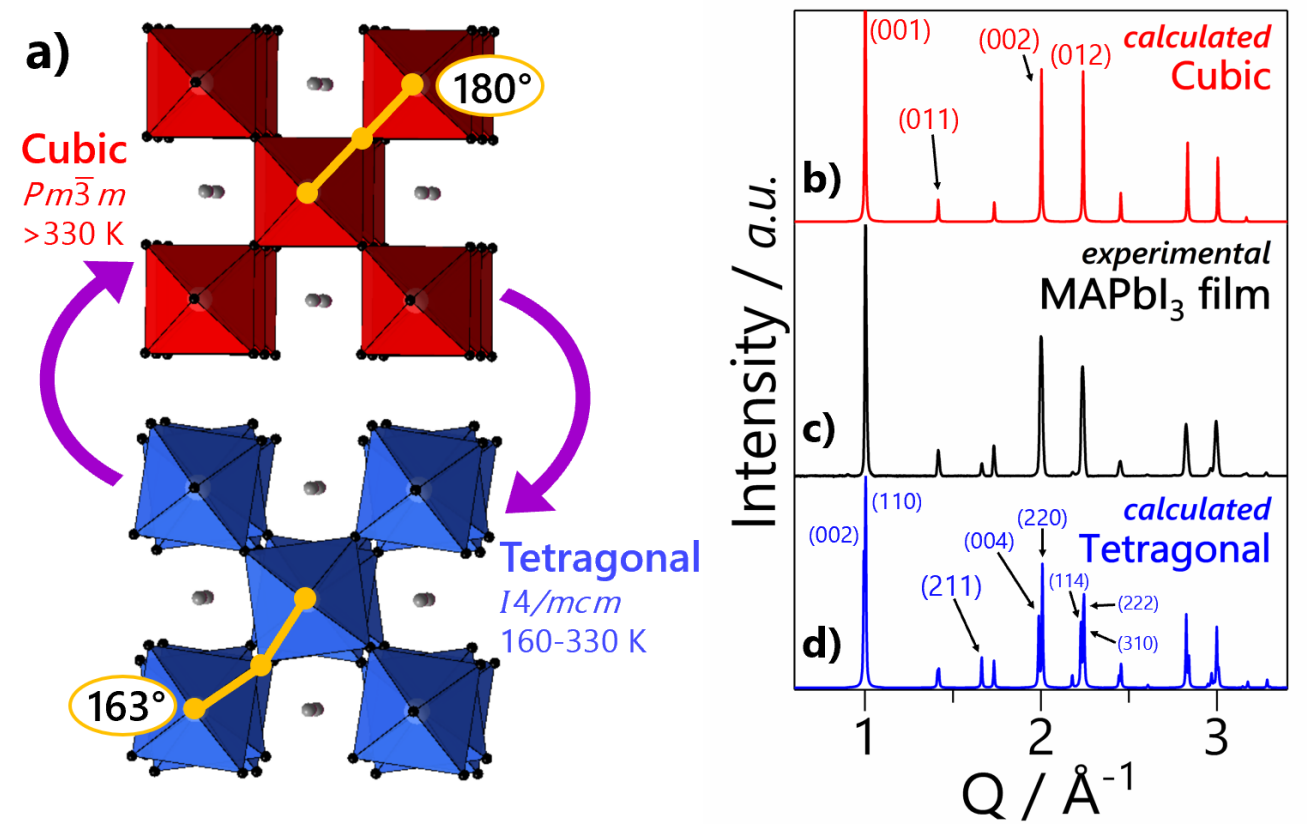


Figure 1. (a) Visualization of the tetragonal (blue) and cubic (red) phases of MAPbI₃. At room temperature and pressure, the material exhibits a tetragonal structure with Pb-I-Pb bond angles that deviate from the ideal octahedron geometry. The gradual extension of these strained bond angles to 180° transforms the material into the cubic perovskite phase. **(b)** Calculated diffraction pattern of the cubic phase (red) of MAPbI₃, **(c)** experimental diffraction pattern of the sample film (black), and **(d)** calculated diffraction pattern of the tetragonal phase (blue) of MAPbI₃. Miller indices are indicated for peaks of interest.

Figure 1 shows steady-state diffraction of the sample (Fig. 1c, black), as well as diffraction patterns calculated from single-crystal X-ray diffraction studies of the high-temperature (>330 K) cubic phase (Fig. 1b, red) and room temperature tetragonal phase (Fig. 1d, blue) of MAPbI₃. The calculated patterns of the tetragonal and cubic phases of MAPbI₃ share many peaks at nearly-identical d-spacings in the experimental film pattern, making it difficult to discern some of the closely-spaced peaks that are present in the tetragonal phase as compared to the cubic phase. However, the lower symmetry of the tetragonal phase results in several additional peaks that are absent in the cubic phase and allow us to distinguish the two phases; the (211) reflection of the

tetragonal phase at $Q = 1.66 \text{ Å}^{-1}$ can be clearly seen in the experimental diffraction pattern (Fig. 1c) and confirms that the unexcited film is in the tetragonal phase.

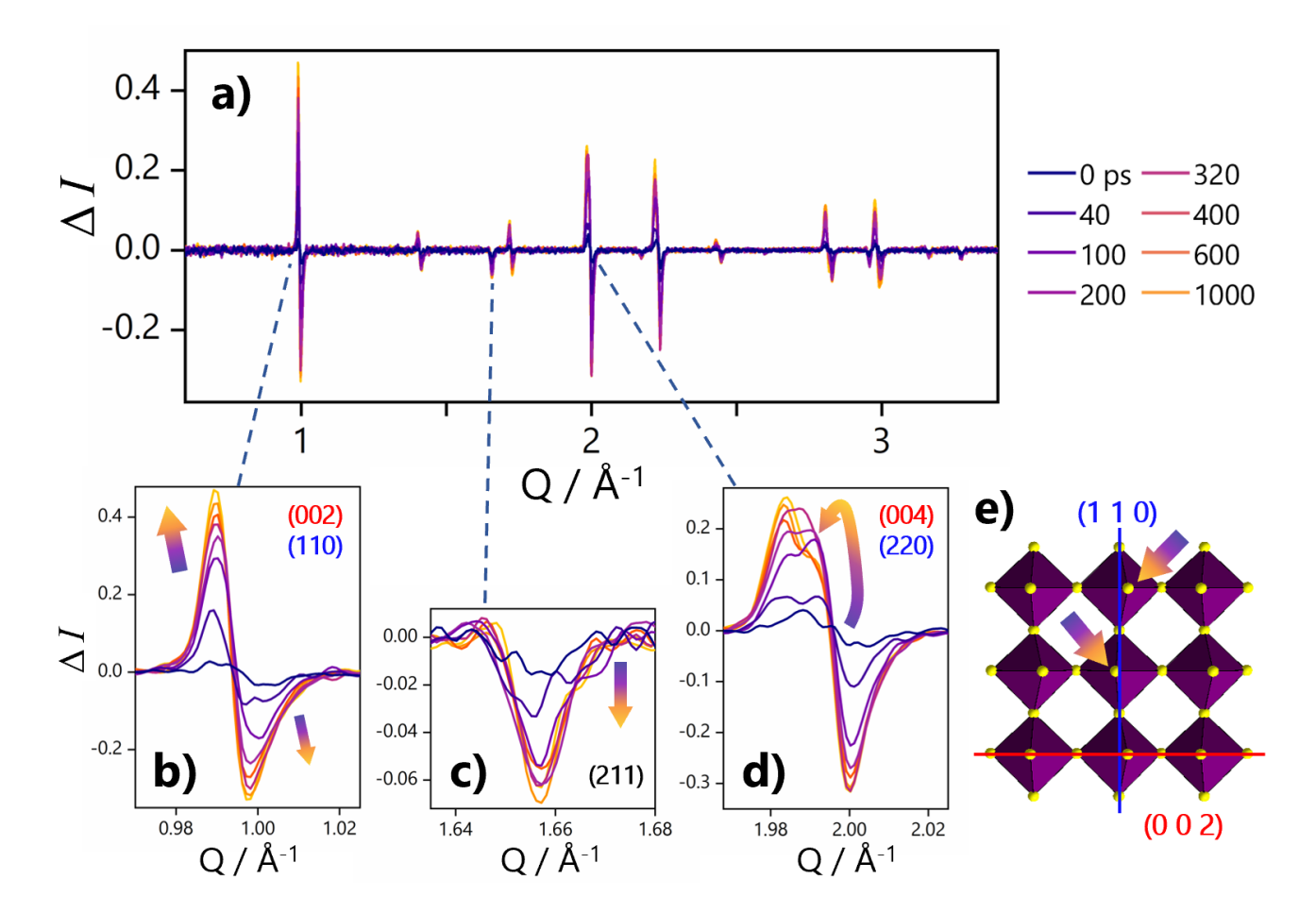


Figure 2. (a) Transient diffraction patterns showing the change in diffraction intensity (Δ*I*) from 0 to 1000 ps (legend at right) at a representative fluence of 77 μJ•cm⁻². Peaks of interest are indicated at Q = 0.99 Å⁻¹, Q = 1.66 Å⁻¹, and Q = 1.99 Å⁻¹. (**b**) Δ*I* centered around Q = 0.99 Å⁻¹ exhibits negative and positive signal at all time delays, indicating lattice expansion. However, the signal shape is asymmetric with the positive signal intensity increasing more quickly than the negative signal over pump-probe delay time. (**c**) Δ*I* at Q = 1.66 Å⁻¹, corresponding to the (211) reflection of the tetragonal phase, decays during the first nanosecond without any evidence of expansion. This reflection is present in the tetragonal phase and absent in the cubic phase. (**d**) Δ*I* centered around Q = 1.99 Å⁻¹ exhibits lattice expansion. In the positive signal, two distinct peaks can be seen increasing in intensity at different rates over time with the area under the positive signal appearing larger than that of the negative signal. (**e**) The (110) and related (*nn*0) family of reflections correspond to the axis along which Pb-I-Pb bond angles are distorted in the tetragonal structure while the (004) and related (002*n*) reflections instead show ideal bonding geometry where the Pb-I-Pb bonds are at or close to 180°.

Transient diffraction patterns collected over the first nanosecond following photoexcitation at a fluence of 77 µJ•cm⁻² are shown in Figure 2. In particular, we observe a reduction of diffraction intensity from the (211) tetragonal reflection at $Q = 1.66 \text{ Å}^{-1}$ over time (Fig. 2c). The decrease in diffraction intensity of this reflection suggests a photoexcited transition of the structure to a higher symmetry space group where the reflection has become systematically absent. Though reflections present only in the tetragonal phase are still observed in the undifferenced transient patterns after photoexcitation, the differenced patterns serve to isolate photoexcited behavior and do not contain information about the unexcited portion of the films. Thus, the absence of positive features at any new positions over time coincident with the isolated reduction in diffraction intensity along tetragonal-only reflections is consistent with the observation of a transition to higher symmetry. Other peaks exhibit both negative and positive features and reach their maximum signal intensity by one nanosecond, suggesting a gradual expansion of the structure along all axes of the lattice (Fig. 2a). Upon lattice expansion, spacing between planes increases and Bragg reflections shift to lower Q values in the diffraction patterns. In transient patterns, these shifts in peak position appear as derivative line shapes with approximately symmetric positive and negative signals at respectively lower and higher Q values. We also note that in contrast to dynamics reported for studies of inorganic colloidal nanoparticle systems, in which structural recovery begins within the instrument response time, the slow rise dynamics of this material that also persist long after the instantaneous formation of charge-carriers are particularly remarkable. ^{23,25-27}

Many peaks in transient patterns also exhibit asymmetric positive and negative signal line shapes. As seen at $Q = 0.99 \text{ Å}^{-1}$ (Fig. 2b), the positive and negative signal intensities are nearly equivalent from 0-60 ps; the positive signal subsequently outgrows the negative signal (Fig. S2). This asymmetry likely arises from higher relative scattering intensities of reflections in the cubic

phase as well as tetragonal reflections disappearing in concert with the appearance of a cubic reflection. Notably, certain regions of transient diffraction patterns exhibit multiple negative and positive features. In Fig. 2d, two distinct features are apparent in the positive signal near Q = 1.99Å⁻¹, indexed to the (004) and (220) Bragg reflections of the tetragonal structure. Initially, the signal intensity corresponding to the (220) reflection on the right increases more quickly than the (004) reflection. However, the (220) begins decaying after 400 ps even as the (004) signal continues to increase until 1 ns. Since these individual reflections are nearly indiscernible in the steady-state pattern (Fig. 1c), the visible peak separation in the transient patterns suggests different magnitudes of expansion along each direction. The (220) reflection corresponds to the lattice plane along which Pb-I-Pb bond angles are distorted away from 180° in the tetragonal structure while the (004) reflection instead results from the lattice plane that exhibits cubic bonding geometry (Fig. 2e), indicating that anisotropic expansion precedes the extension of the distorted bond angles within the first nanosecond following excitation. Similar changes in diffraction intensity are observed in other reflections that overlap in the steady-state pattern including those at $Q = 2.23 \text{ Å}^{-1}$ which are discussed in further detail below (Figure 3a,b). This complex evolution has not been reported in the mechanism of the first-order thermodynamic transition. Though the properties of the first-order phase transition at 330 K in MAPbI₃ have been well-characterized, previous empirical studies have not examined transient diffraction patterns of MAPbI₃, such as those reported here, due to the ultrafast experimental conditions required. As a non-equilibrium phenomenon, these observations are consistent with reports of preferential coupling and polaron formation along the c-axis in both computational and experimental studies of metal halide perovskites. 6,7,28

Additionally, the positive signal retains a shoulder feature around $Q = 1.99 \text{ Å}^{-1}$ where the (220) reflection appears. We considered that the lingering (220) feature may be due to many

distinct lattice domains throughout the film that exhibit different degrees of structural distortion over time.²⁹ In addition to the tetragonal and cubic structures, local distortions with sufficient coherence would result in distinct diffraction features as pump-probe delay time increases since carriers and heat likely diffuse into domains below the photoexcited population subsequent to the initial photoexcitation pulse.³⁰ As the local structure expands and distorts to accommodate the inflow of carriers and thermal energy, these populations would begin to appear as an additional feature, such as the shoulder noted above, in the transient pattern.

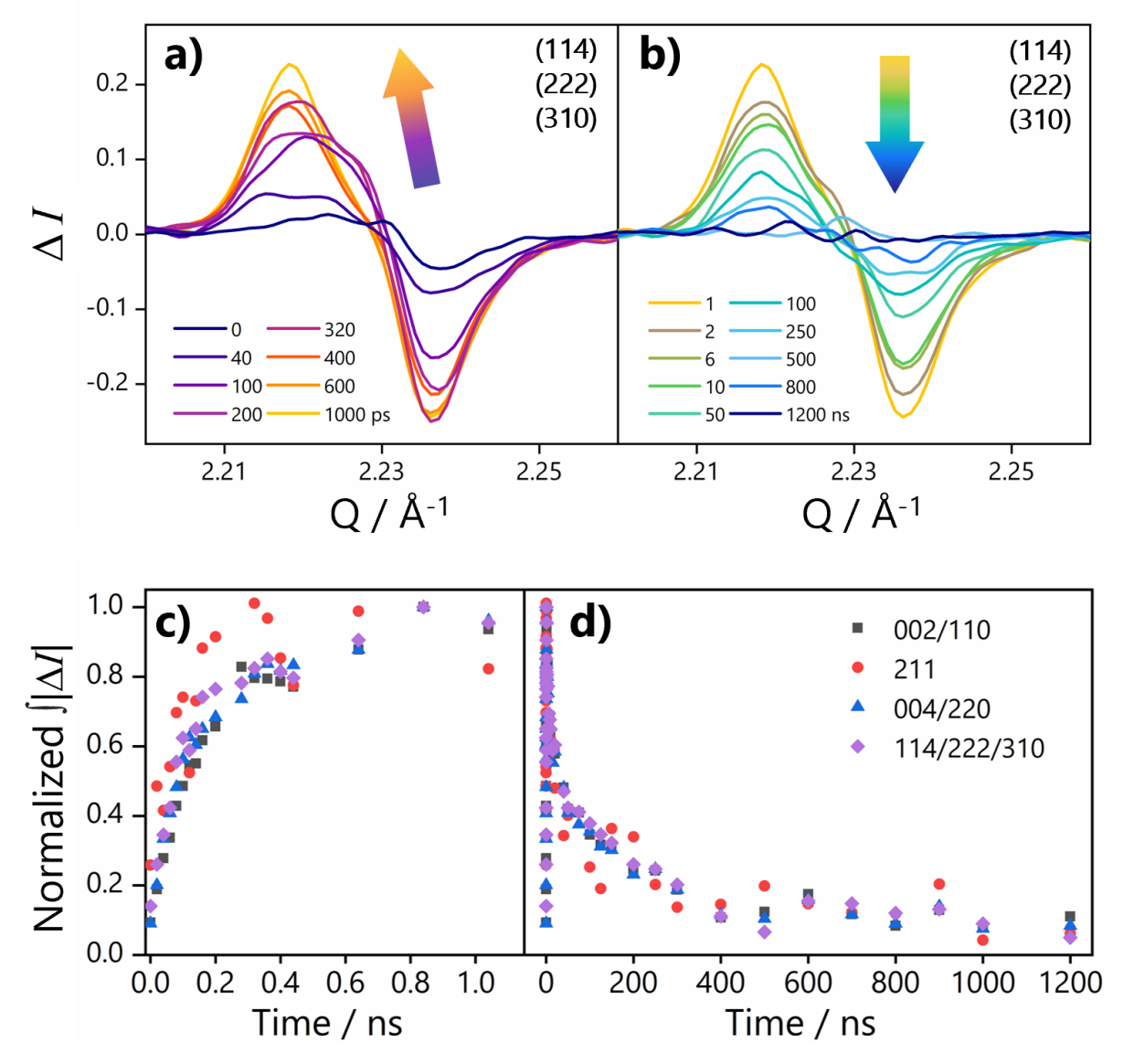


Figure 3. At top, transient patterns at 77 μJ • cm⁻² showing the change in diffraction intensity (ΔI) centered around Q = 2.23 Å⁻¹ from (a) 0 to 1 ns and (b) 0 to 1200 ns following photoexcitation. At bottom, normalized integrated absolute values of peak areas ($\int |\Delta I|$) as a function of pump-probe delay time for selected reflections from (c) 0 to 1 ns and (d) 0 to 1200 ns following photoexcitation. Exponential fitting of normalized $\int |\Delta I|$ with respect to time revealed fluence-averaged "rise" lifetimes of $\tau_{2II} = 144 \pm 20$ ps for the initial decrease of (211) reflection (red, circle) as well as $\tau_I = 58 \pm 10$ ps and $\tau_2 = 296 \pm 26$ ps for the remaining peaks. Following 1 ns, the structure begins its "recovery" with fluence-averaged fitted lifetimes of $\tau_3 = 11.1 \pm 4.1$ ns and $\tau_4 = 236 \pm 49$ ns.

After 1 ns, pump-induced changes in X-ray diffraction intensity begin to decrease across all reflections, indicating structural relaxation and contraction as well as recovery toward the unperturbed lattice phase. Interestingly, in Figure 3a we observe multiple features – indexed to the

(114), (222), and (310) Bragg reflections of the tetragonal phase – evolving at different rates, especially noting the dominant shoulder at high Q values in the positive lobe at early times. In contrast, the line shape at all times after the material begins to relax exhibits wholly new features (Fig. 3b). The three indexed reflections appear less distinguishable, and the dominant shoulder at $Q = 2.225 \text{ Å}^{-1}$ does not re-appear with the same diffraction intensity. The transition mechanism of the material from tetragonal to cubic appears to differ from the recovery mechanism back to the initial tetragonal phase. In order to elucidate the origins of this mechanistic hysteresis and other observed structural evolutions, we examine the dynamics of these phenomena and identify correlated behaviors as potential sources.

Dynamics were further investigated by calculating the absolute value of the integrated area of the transient pattern at each pump-probe delay. The rise and recovery dynamics for selected peaks at a representative fluence of 77 μ J•cm⁻² are shown in Figure 3c. The (211) tetragonal reflection at Q = 1.66 Å⁻¹ displayed single exponential behavior with an average lifetime of τ_{211} = 144 ± 20 ps across all measured fluences with sufficient intensity for fitting (Fig. S3). However, biexponential fitting of the rise in diffraction signal across the other selected peaks and fluences (Fig. 3c) indicated two processes: an initial, rapid response over tens of picoseconds (τ_1 = 58 ± 10 ps) followed by a longer rise lifetime over hundreds of picoseconds (τ_2 = 296 ± 26 ps). The fitted values for τ_1 fall within the pulsewidth of the X-ray probe and may correlate to reports of acoustic phonon lifetimes¹⁹ and thermal bottlenecking³¹ while the longer lifetimes τ_2 correlate with both polaron stabilization lifetimes⁴ (~300 ps) and thermalization lifetimes^{32,33} (~250 ps) found between the organic and inorganic lattice in transient, optical studies. Biexponential fitting of the recovery dynamics averaged across all measured fluences (Fig. 3d) showed a decay of τ_3 = 11.1 ± 4.1 ns followed by a slower relaxation of τ_4 = 236 ± 49 ns for all analyzed peaks, the latter of which

outlives several reports of radiative recombination lifetimes in similar MAPbI₃ films and points to the metastability and hindered recovery of the excited state structure.^{34,35} The faster recovery timescale τ_3 correlates with carrier relaxation and recombination timescales,^{1,14} while the slower recovery τ_4 process shows the transient signals becoming weaker, suggesting lattice contraction and cooling.

The anisotropic rates of change along each direction of the lattice are consistent with reports that the formation and stabilization of polarons occurs preferentially along the c-axis – elongating the lattice in the (00*l*) direction (see Fig. 2e) – followed by straightening of the distorted Pb-I-Pb bonds into the cubic phase. Prior reports have found that photoexcited electrons couple preferentially with phonons corresponding to the stretching and bending of Pb-I-Pb bonds; this electron-phonon coupling enables polaron formation to occur along the c-axis where the electrons couple with Pb-I bond vibrations. Guzelturk et al. conducted transient single crystal X-ray diffraction studies in the related hybrid perovskite methylammounium lead bromide and observed similar anisotropic strain associated with electronic changes, estimating the strain energies and finding them in agreement with polaron binding energies and estimated polaron radius.^{9,36} However, the dissipation of polarons with lifetimes of hundreds of picoseconds in related metal halide materials, 6 significantly shorter than τ_4 in this work, may restrict relaxation pathways and thus contribute to the prolonged metastability of the excited structure as well as observed hysteresis in the transition mechanism. It is also likely that the rapid absorption of photons and subsequent non-equilibrium behavior induces strain in the material that impacts the onset of the phase transition.³⁷ As such, there would be lattice distortions that accommodate the interface between the photoexcited population against the unexcited population of the sample.³⁸

Ranges of temperature elevation of the photoexcited material were calculated as a function of pump fluence (Table S1).^{8,39} Maximum temperature calculations assumed all pump energy became available thermal energy, while minimum temperatures were calculated assuming only photon energy in excess of the band gap is dissipated thermally. Additional details are available in the Supporting Information. We note that these calculations do not consider thermal diffusion into the rest of the film over time and thus represent the effective temperature of only the photoexcited material at early time. 2,30,40,41 Calculated effective temperatures fall short of the reported temperature at which a phase transition occurs (330 K) for all but the highest fluence studied in this work (413 µJ•cm⁻²). This suggests that the phase transition toward the cubic phase is primarily drive by the presence of charge-carriers. In this respect, previous reports examining the calculated band structure of MAPbI₃ have observed that the highest occupied states of the valence band are primarily composed of nonbonding and anti-bonding molecular orbitals that are stabilized by the hydrogen bonding between the methylammonium cation and octahedral iodide, contributing to the octahedral distortions observed in the tetragonal phase. 42,43 Thus, promoting an electron from the valence band maximum to the conduction band minimum may relax these distortions both by inducing organic cation motion that breaks the stabilizing hydrogen bonding, as recent ultrafast structural studies of metal halides materials have observed on picosecond timescales, while also strengthening the bonding orbitals in the Pb-I-Pb bonds that results in the relaxation of the octahedral distortions. 21,44

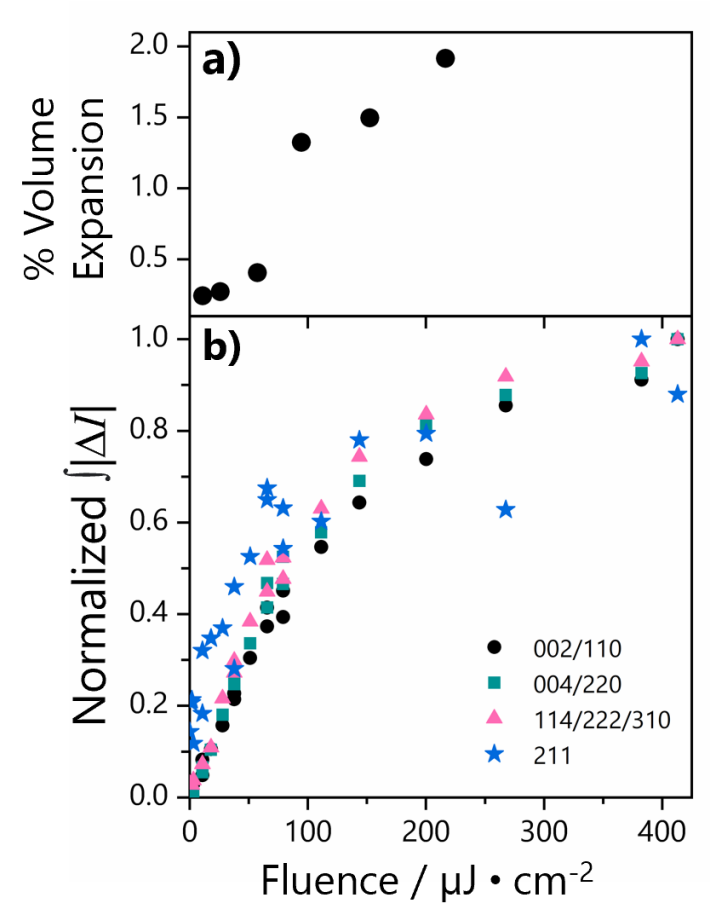


Figure 4. (a) Percent volume expansion of the photoexcited structure at 1 ns compared to the equilibrium cubic structure at 330 K. **(b)** Normalized integrated absolute values of peak areas $\int |\Delta I|$ as a function of pump fluence for selected reflections.

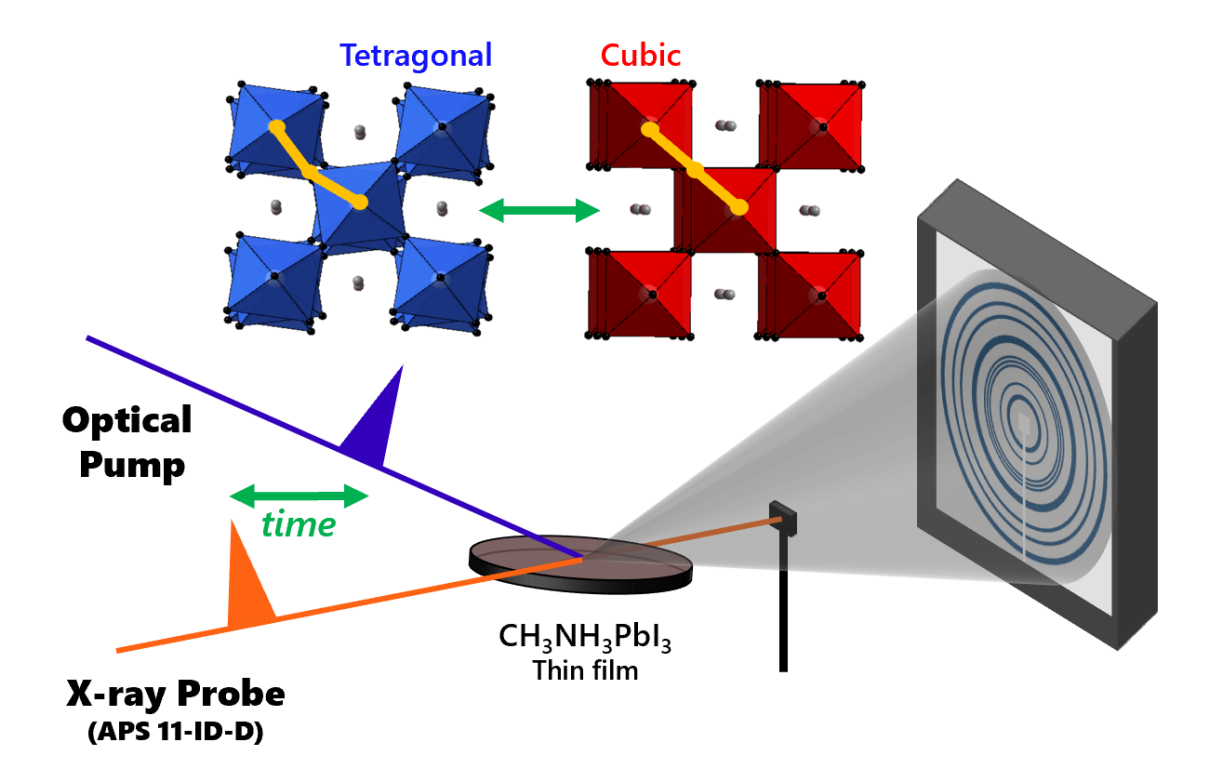
Importantly, many of the dynamic responses observed herein show pump fluence-independent behaviors in the limit of low fluence (at or below $\sim 100~\mu J \cdot cm^{-2}$). Because the data shows that lifetimes are quantitatively independent of the number of photons with which we have excited the sample at low power, it is reasonable to suggest that such response occurs for wide-ranging optoelectronic applications, including solar cells. While the timescales of structural changes are fluence-independent at or below this fluence, all analyzed peaks exhibit fluence-dependent signal intensity, rising linearly up to $100~\mu J \cdot cm^{-2}$ and then exhibiting saturation at higher fluences (Figure 4b). Given that Auger recombination becomes important for carriers at reported

fluences close to \sim 3-10 uJ·cm⁻² and results in an appreciable increase in available thermal energy, $^{1.14,34}$ this unexpected trend at low fluences also suggests that lattice heating from non-radiative relaxation pathways is not chiefly responsible for the phase transition mechanism. Features from the transient patterns at 1 ns after excitation for selected fluences were indexed to $Pm\overline{3}m$, the same reported space group as the known cubic structure of MAPbI₃. The observed diffraction intensities for this higher symmetry structure are consistent with the known, thermodynamically-accessible cubic structure of MAPbI₃, thus we assign the cubic space group to the photoexcited structures at maximum signal intensity and acknowledge that this assignment may simplify the true excited structure owing to evaluation of a time-averaged response. Unexpectedly, the unit cell volumes were larger than reported values for the known, thermodynamic cubic phase at the phase transition temperature of 330 K (Fig. 4a). Though these transient expanded cubic parameters may also occur at higher temperatures, the structures observed here are non-equilibrium structures near room temperature. The presence of charge-carriers, then, likely accounts for the additional lattice expansion observed.

This is the first report that directly measures the *in-situ* operative structure of MAPbI₃, as well as its dynamic behavior, under optical stimulation. We also notably identify several non-equilibrium structures and phenomena that have not been shown in studies where the structure is measured in equilibrium. Using ultrafast X-ray diffraction techniques, we identified and characterized the dynamic, photoexcited structures of MAPbI₃. We observed anisotropic distortions and rates of change along specific directions of the lattice as the material transitions from the starting phase to a higher-symmetry, metastable excited structure over 1 ns following photoexcitation. We also observed hysteresis between the rise and recovery behaviors of the non-equilibrium phase transition, and we consider that the dynamic formation, stabilization, and

dissipation of polarons along the *c*-axis of the lattice may be responsible. These structural changes have not been observed in the tetragonal-to-cubic phase transition in MAPbI₃, let alone at the low effective temperatures calculated in this study, indicating that these behaviors cannot be explained only by an increase in thermal energy due to photoexcitation. In this regard, a key aspect of future work will be to understand the quantitative contributions from each of the various energetic components that comprise the material's structural response to photoexcitation. This includes, but is not limited to, the thermal dissipation of incoming photon energy. Manipulating the excitation pump energies and ambient experimental temperatures can affect the kinetics of hot-carrier relaxation and Auger processes, advancing our understanding of photoexcited structural reorganization in hybrid perovskite materials. The dynamics of these non-equilibrium structures demonstrate the flexible lattice response of metal halide perovskites that facilitates favorable properties and provide further insight to enable new device architectures for both photovoltaics and novel applications that exploit ultrafast, non-equilibrium symmetry switches, such as quantum computing and information sciences.

TOC Figure



Acknowledgements

We acknowledge student support provided by the National Science Foundation under Grant No. MSN-1808590. Work performed at the Center for Nanoscale Materials and Advanced Photon Source, both U.S. Department of Energy Office of Science User Facilities, was supported by the U.S. DOE, Office of Basic Energy Sciences, under Contract No. DE-AC02-06CH11357. M.G.K. acknowledges support from the US Department of Energy, Office of Science Grant No. SC0012541. L.X.C. acknowledges the support from Solar Energy and Photochemistry Program, Basic Energy Science, US Department of Energy, under Contract No. DE-AC02-06CH11357. This work used the IMSERC X-ray facility at Northwestern University which receives support from the Soft and Hybrid Nanotechnology Experimental (SHyNE) Resource (NSF ECCS-2025633) and Northwestern University. This work made use of the GIANTFab core facility at Northwestern University. GIANTFab is supported by the Institute for Sustainability and Energy at Northwestern University. GIANTFab is supported by the Institute for Sustainability and Energy at Northwestern and the Office of the Vice President for Research at Northwestern. S.P. gratefully acknowledges support from the NSF Graduate Research Fellowship Program under Grant No. DGE-1842165 and the Ryan Fellowship.

Supporting Information

The Supporting Information is available for free of charge at XXX Experimental and data processing methods including sample fabrication, beamline setup, temperature estimations, and additional data figures and tables (Fig. S1-S3, Table S1)

References

- Herz, L. M. Charge-Carrier Dynamics in Organic-Inorganic Metal Halide Perovskites. *Annual Review of Physical Chemistry* **67**, 65-89 (2016). https://doi.org:10.1146/annurev-physchem-040215-112222
- Johnston, M. B. & Herz, L. M. Hybrid Perovskites for Photovoltaics: Charge-Carrier Recombination, Diffusion, and Radiative Efficiencies. *Accounts of Chemical Research* **49**, 146-154 (2016). https://doi.org:10.1021/acs.accounts.5b00411
- Brenner, T. M., Egger, D. A., Kronik, L., Hodes, G. & Cahen, D. Hybrid organic—inorganic perovskites: low-cost semiconductors with intriguing charge-transport properties. *Nature Reviews Materials* 1, 15007 (2016). https://doi.org:10.1038/natrevmats.2015.7
- 4 Miyata, K., Atallah, T. L. & Zhu, X.-Y. Lead halide perovskites: Crystal-liquid duality, phonon glass electron crystals, and large polaron formation. *Science Advances* **3**, e1701469 (2017). https://doi.org:doi:10.1126/sciadv.1701469
- 5 Panzer, F., Li, C., Meier, T., Köhler, A. & Huettner, S. Impact of Structural Dynamics on the Optical Properties of Methylammonium Lead Iodide Perovskites. *Advanced Energy Materials* **7**, 1700286 (2017). https://doi.org:10.1002/aenm.201700286
- Guzelturk, B. *et al.* Visualization of dynamic polaronic strain fields in hybrid lead halide perovskites. *Nature Materials* **20**, 618-623 (2021). https://doi.org:10.1038/s41563-020-00865-5
- Schlipf, M., Poncé, S. & Giustino, F. Carrier Lifetimes and Polaronic Mass Enhancement in the Hybrid Halide Perovskite CH₃NH₃PbI₃ from Multiphonon Frohlich Coupling. *Physical Review Letters* **121**, 086402 (2018). https://doi.org:10.1103/PhysRevLett.121.086402
- 8 Yang, Y. *et al.* Observation of a hot-phonon bottleneck in lead-iodide perovskites. *Nature Photonics* **10**, 53-59 (2016). https://doi.org;10.1038/nphoton.2015.213
- Frost, J. M., Whalley, L. D. & Walsh, A. Slow Cooling of Hot Polarons in Halide Perovskite Solar Cells. *ACS Energy Letters* **2**, 2647-2652 (2017). https://doi.org:10.1021/acsenergylett.7b00862
- Quarti, C. *et al.* Structural and optical properties of methylammonium lead iodide across the tetragonal to cubic phase transition: implications for perovskite solar cells. *Energy & Environmental Science* **9**, 155-163 (2016). https://doi.org/10.1039/C5EE02925B
- Rolston, N. *et al.* Comment on "Light-induced lattice expansion leads to high-efficiency perovskite solar cells". *Science* **368**, eaay8691 (2020). https://doi.org/doi:10.1126/science.aay8691
- Zhu, H. *et al.* Screening in crystalline liquids protects energetic carriers in hybrid perovskites. *Science* **353**, 1409-1413 (2016). https://doi.org:10.1126/science.aaf9570
- Diroll, B. T. Temperature-Dependent Intraband Relaxation of Hybrid Perovskites. *The Journal of Physical Chemistry Letters* **10**, 5623-5628 (2019). https://doi.org/10.1021/acs.jpclett.9b02320
- Allegro, I. *et al.* Bimolecular and Auger Recombination in Phase-Stable Perovskite Thin Films from Cryogenic to Room Temperature and Their Effect on the Amplified Spontaneous Emission Threshold. *The Journal of Physical Chemistry Letters* **12**, 2293-2298 (2021). https://doi.org:10.1021/acs.jpclett.1c00099
- Hopper, T. R. *et al.* Ultrafast Intraband Spectroscopy of Hot-Carrier Cooling in Lead-Halide Perovskites. *ACS Energy Letters* **3**, 2199-2205 (2018). https://doi.org.10.1021/acsenergylett.8b01227
- Jacobsson, T. J., Schwan, L. J., Ottosson, M., Hagfeldt, A. & Edvinsson, T. Determination of Thermal Expansion Coefficients and Locating the Temperature-Induced Phase Transition in Methylammonium Lead Perovskites Using X-ray Diffraction. *Inorganic Chemistry* **54**, 10678-10685 (2015). https://doi.org;10.1021/acs.inorgchem.5b01481
- 17 Verma, S. D., Gu, Q., Sadhanala, A., Venugopalan, V. & Rao, A. Slow Carrier Cooling in Hybrid Pb–Sn Halide Perovskites. *ACS Energy Letters* **4**, 736-740 (2019). https://doi.org:10.1021/acsenergylett.9b00251
- Poglitsch, A. & Weber, D. Dynamic disorder in methylammoniumtrihalogenoplumbates (II) observed by millimeter-wave spectroscopy. *The Journal of Chemical Physics* **87**, 6373-6378 (1987). https://doi.org:10.1063/1.453467

- Whitfield, P. S. *et al.* Structures, Phase Transitions and Tricritical Behavior of the Hybrid Perovskite Methyl Ammonium Lead Iodide. *Scientific Reports* **6**, 35685 (2016). https://doi.org:10.1038/srep35685
- Stoumpos, C. C., Malliakas, C. D. & Kanatzidis, M. G. Semiconducting Tin and Lead Iodide Perovskites with Organic Cations: Phase Transitions, High Mobilities, and Near-Infrared Photoluminescent Properties. *Inorganic Chemistry* **52**, 9019-9038 (2013). https://doi.org:10.1021/ic401215x
- Wu, X. *et al.* Light-induced picosecond rotational disordering of the inorganic sublattice in hybrid perovskites. *Science Advances* **3**, e1602388 (2017). https://doi.org/doi:10.1126/sciadv.1602388
- Harmand, M. *et al.* Achieving few-femtosecond time-sorting at hard X-ray free-electron lasers. *Nature Photonics* 7, 215-218 (2013). https://doi.org:10.1038/nphoton.2013.11
- Kirschner, M. S. *et al.* Photoinduced, reversible phase transitions in all-inorganic perovskite nanocrystals. *Nature Communications* **10**, 504 (2019). https://doi.org/10.1038/s41467-019-08362-3
- Tsai, H. *et al.* High-efficiency two-dimensional Ruddlesden–Popper perovskite solar cells. *Nature* **536**, 312-316 (2016). https://doi.org:10.1038/nature18306
- Kirschner, M. S. *et al.* Transient Melting and Recrystallization of Semiconductor Nanocrystals Under Multiple Electron–Hole Pair Excitation. *Nano Letters* **17**, 5314-5320 (2017). https://doi.org:10.1021/acs.nanolett.7b01705
- Harvey, S. M. *et al.* Transient Lattice Response upon Photoexcitation in CuInSe2 Nanocrystals with Organic or Inorganic Surface Passivation. *ACS Nano* **14**, 13548-13556 (2020). https://doi.org:10.1021/acsnano.0c05553
- Brumberg, A. *et al.* Anisotropic Transient Disordering of Colloidal, Two-Dimensional CdSe Nanoplatelets upon Optical Excitation. *Nano Letters* **21**, 1288-1294 (2021). https://doi.org:10.1021/acs.nanolett.0c03958
- Ghosh, D., Welch, E., Neukirch, A. J., Zakhidov, A. & Tretiak, S. Polarons in Halide Perovskites: A Perspective. *The Journal of Physical Chemistry Letters* **11**, 3271-3286 (2020). https://doi.org:10.1021/acs.jpclett.0c00018
- 29 Snaider, J. M. *et al.* Ultrafast Imaging of Carrier Transport across Grain Boundaries in Hybrid Perovskite Thin Films. *ACS Energy Letters* **3**, 1402-1408 (2018). https://doi.org:10.1021/acsenergylett.8b00560
- Jiang, X., Hoffman, J., Stoumpos, C. C., Kanatzidis, M. G. & Harel, E. Transient Sub-Band-Gap States at Grain Boundaries of CH3NH3PbI3 Perovskite Act as Fast Temperature Relaxation Centers. *ACS Energy Letters* **4**, 1741-1747 (2019). https://doi.org:10.1021/acsenergylett.9b00885
- Gold-Parker, A. *et al.* Acoustic phonon lifetimes limit thermal transport in methylammonium lead iodide. *Proceedings of the National Academy of Sciences* **115**, 11905-11910 (2018). https://doi.org.doi:10.1073/pnas.1812227115
- Chang, A. Y. *et al.* Slow Organic-to-Inorganic Sub-Lattice Thermalization in Methylammonium Lead Halide Perovskites Observed by Ultrafast Photoluminescence. *Advanced Energy Materials* **6**, 1600422 (2016). https://doi.org:10.1002/aenm.201600422
- Guo, P. *et al.* Slow thermal equilibration in methylammonium lead iodide revealed by transient mid-infrared spectroscopy. *Nature Communications* **9**, 2792 (2018). https://doi.org:10.1038/s41467-018-05015-9
- Davies, C. L. *et al.* Bimolecular recombination in methylammonium lead triiodide perovskite is an inverse absorption process. *Nature Communications* **9**, 293 (2018). https://doi.org.10.1038/s41467-017-02670-2
- Crothers, T. W. *et al.* Photon Reabsorption Masks Intrinsic Bimolecular Charge-Carrier Recombination in CH3NH3PbI3 Perovskite. *Nano Letters* **17**, 5782-5789 (2017). https://doi.org:10.1021/acs.nanolett.7b02834
- Zheng, F. & Wang, L.-w. Large polaron formation and its effect on electron transport in hybrid perovskites. *Energy & Environmental Science* **12**, 1219-1230 (2019). https://doi.org:10.1039/C8EE03369B

- Zhao, J. *et al.* Strained hybrid perovskite thin films and their impact on the intrinsic stability of perovskite solar cells. *Science Advances* **3**, eaao5616 (2017). https://doi.org:doi:10.1126/sciadv.aao5616
- Kennard, R. M. *et al.* Ferroelastic Hysteresis in Thin Films of Methylammonium Lead Iodide. *Chemistry of Materials* **33**, 298-309 (2021). https://doi.org:10.1021/acs.chemmater.0c03776
- Onoda-Yamamuro, N., Matsuo, T. & Suga, H. Calorimetric and IR spectroscopic studies of phase transitions in methylammonium trihalogenoplumbates (II). *Journal of Physics and Chemistry of Solids* **51**, 1383-1395 (1990). https://doi.org;10.1016/0022-3697(90)90021-7
- Qian, X., Gu, X. & Yang, R. Lattice thermal conductivity of organic-inorganic hybrid perovskite CH3NH3PbI3. *Applied Physics Letters* **108**, 063902 (2016). https://doi.org:10.1063/1.4941921
- Nah, S. *et al.* Spatially segregated free-carrier and exciton populations in individual lead halide perovskite grains. *Nature Photonics* **11**, 285-288 (2017). https://doi.org:10.1038/nphoton.2017.36
- Lee, J.-H. *et al.* Resolving the Physical Origin of Octahedral Tilting in Halide Perovskites. *Chemistry of Materials* **28**, 4259-4266 (2016). https://doi.org:10.1021/acs.chemmater.6b00968
- Lee, J.-H., Bristowe, N. C., Bristowe, P. D. & Cheetham, A. K. Role of hydrogen-bonding and its interplay with octahedral tilting in CH3NH3PbI3. *Chemical Communications* **51**, 6434-6437 (2015). https://doi.org:10.1039/C5CC00979K
- Cannelli, O. *et al.* Quantifying Photoinduced Polaronic Distortions in Inorganic Lead Halide Perovskite Nanocrystals. *Journal of the American Chemical Society* **143**, 9048-9059 (2021). https://doi.org:10.1021/jacs.1c02403

The submitted manuscript has been created by UChicago Argonne, LLC, Operator of Argonne National Laboratory ("Argonne"). Argonne, a U.S. Department of Energy Office of Science laboratory, is operated under Contract No. DE-AC02-06CH11357. The U.S. Government retains for itself, and others acting on its behalf, a paid-up nonexclusive, irrevocable worldwide license in said article to reproduce, prepare derivative works, distribute copies to the public, and perform publicly and display publicly, by or on behalf of the Government. The Department of Energy will provide public access to these results of federally sponsored research in accordance with the DOE Public Access Plan. http://energy.gov/downloads/doe-public-access-plan